HHS Public Access

Author manuscript

Nat Neurosci. Author manuscript; available in PMC 2018 December 18.

Published in final edited form as:

Nat Neurosci. 2018 July ; 21(7): 963–973. doi:10.1038/s41593-018-0167-4.

The locus coeruleus drives disinhibition in the midline thalamus via a dopaminergic mechanism

B. Sofia Beas[1,*], **Brandon J. Wright**[1,*], **Miguel Skirzewski**[2], **Yan Leng**[1], **Jung Ho Hyun**[3], **Omar Koita**[1], **Nicholas Ringelberg**[1], **Hyung-Bae Kwon**[3,4], **Andres Buonanno**[2], and **Mario A. Penzo**[1,#]

[1]National Institute of Mental Health, Bethesda, MD 20850

[2]National Institute of Child Health and Human Development, Bethesda, MD 20850

[3]Max Planck Florida Institute for Neuroscience, Jupiter, Florida 33458, USA

[4]Max Planck Institute of Neurobiology, Martinsried 82152, Germany

Abstract

The paraventricular nucleus of the thalamus (PVT) is increasingly being recognized as a critical node linking stress detection to the emergence of adaptive behavioral responses to stress. However, despite growing evidence implicating the PVT in stress processing, the neural mechanisms by which stress impacts PVT neurocircuitry and promotes stressed states remain unknown. Here we show that stress exposure drives a rapid and persistent reduction of inhibitory transmission onto projection neurons of the posterior PVT (pPVT). This stress-induced disinhibition of the pPVT was associated with a locus coeruleus (LC)-mediated rise in the extracellular concentration of dopamine in the midline thalamus, required the function of dopamine D2 receptors on PVT neurons and increased sensitivity to stress. Our findings define the LC as an important modulator of PVT function: by controlling the inhibitory tone of the pPVT, it modulates the excitability of pPVT projection neurons and controls stress responsivity.

Keywords

Paraventricular thalamus; stress; dopamine D2 receptor; locus coeruleus

[#]Correspondence: Mario A. Penzo, PhD., Unit on the Neurobiology of Affective Memory, National Institute of Mental Health, 35 Convent Drive, Bldg. 35A Room 2E621, Bethesda, MD 20850., mario.penzo@nih.gov.

[*]These authors contributed equally to this work

AUTHOR CONTRIBUTIONS

B.S.B. performed anatomical and immunohistochemical studies, calcium and chloride imaging experiments, optogenetic experiments, and stereotaxic injections for all experiments. B.J.W. and M.A.P. performed electrophysiological experiments. M.S. performed microdialysis experiments and analyzed collected fractions via HPLC. Y.L. performed RT-PCR and in situ hybridization experiments. J.H.H. performed all procedures for two-photon imaging of gephyrin puncta. O.K. and N.R. performed stereotaxic surgeries and histological procedures. A.B. and H.B.K. provided critical reagents and suggestions. B.S.B., B.J.W. and M.A.P. designed the study, interpreted results and wrote the paper.

COMPETING INTERESTS

The authors declare no competing financial interests.

The paraventricular nucleus of the thalamus (PVT), a stress-sensitive region located in the dorsal part of the midline thalamus[1], has been heavily implicated in signaling aversive states[2]. More recently, studies employing optogenetic and chemogenetic approaches linked specific projections of the PVT to selected behavioral responses to stress[3–6]. Thus, whereas amygdala-projecting neurons of the PVT participate in the formation and retrieval of fear memory[3,4], those that project to the nucleus accumbens (NAc) are thought to control drug and food seeking behaviors following opiate withdrawal and food restriction, respectively[5,6]. However, despite substantial improvements in our understanding of how different outputs of the PVT guide behavioral responses to stress, the cellular and circuit mechanisms that regulate the activity of the PVT during stressed states are far less clear. As a result, a comprehensive picture of how modulatory systems are integrated in the PVT to impact its overall function in stress-related behaviors is lacking.

While resembling most other thalamic nuclei, such that it lacks GABAergic interneurons[7], the rodent PVT is known to receive multiple extrathalamic GABAergic afferents arising from a wide range of brain areas that include the zona incerta[8], the hypothalamus[9], and the pontine reticular formation[10]. Structural analyses of inhibitory afferents to intralaminar and midline nuclei of the thalamus reveal unique large multi-synaptic terminals that are conserved across several species[10–12]. Consequently, thalamic neurons that receive extrathalamic inhibitory afferents display strong spontaneous synaptic inhibition as well as attenuated short-term synaptic plasticity[10,12]. Overall, the features of extrathalamic inhibitory afferents point to a strong and focal inhibitory system and highlight the importance of circuit and cellular mechanisms underlying disinhibition[13]. As a validation of this model, here we show that stress results in the rapid and persistent dopamine-mediated disinhibition of projection neurons of the posterior PVT (pPVT), which is driven by input from the locus coeruleus (LC) and promotes stress responsivity. Our results uncover a previously unknown cellular and circuit mechanism that shapes PVT responses to stress, thereby controlling the emergence of stress-related behaviors.

RESULTS

Stress drives inhibitory plasticity in the pPVT

The PVT is the target of diverse and widespread inhibitory inputs (Supplementary Fig. 1), suggesting that despite the lack of local interneurons, GABAergic inhibition plays a prominent role in the control of PVT function. Thus, to assess the effect of stress on inhibitory transmission in the pPVT, we performed *ex vivo* voltage clamp recordings from GFP-fluorescent neurons of *Drd2*-EGFP mice – where most projection neurons of the pPVT are labeled by EGFP (Supplementary Fig. 2) – and compared the frequency and amplitude of miniature inhibitory postsynaptic currents (mIPSC) between naïve and stressed mice (Fig. 1a–d). We observed a significant effect of stress on inhibitory synaptic transmission in $D2^{+}$ neurons of the pPVT (Fig. 1b–d). This stress-mediated effect on inhibitory transmission was accounted for as a significant decrease in the average amplitude of mIPSC, observed at 2h and 24h after stress (Fig. 1b, d). A non-significant decrease in mIPSC frequency was also observed at 24h after stress (Fig. 1c). Altogether, these findings suggest that stress-induced inhibitory plasticity is likely to be mediated by predominantly postsynaptic

mechanisms[14–16]. As there are known sex differences in stress susceptibility[17,18], we used both male and female mice in this experiment to determine if stress-induced disinhibition varies across sex. For this, we separately analyzed data gathered from neurons of *Drd2*-EGFP mice of each sex and observed near identical inhibitory transmission across different experimental conditions (Supplementary Fig. 3). Thus, we assumed that synaptic inhibition in the pPVT was similarly impacted in both sexes and did not repeat this type of analysis on the remaining experiments (although both males and females were included throughout this study [Supplementary Table 1]). Next, to investigate the *in vivo* dynamics of stress-evoked disinhibition, we used fiber photometry to monitor changes in intracellular chloride in projection neurons of the pPVT (Fig. 1e). To achieve this, we restricted the expression of the genetically-encoded chloride sensor SuperClomeleon[19], to NAc-projecting neurons of the pPVT (Fig. 1f), since a vast majority of projection neurons of the pPVT innervate the NAc[20]. SuperClomeleon is a fluorescence resonance energy transfer (FRET)-based sensor (see methods) in which chloride quenches the fluorescence of the yellow fluorescent protein (YFP). Therefore, changes in the ratio between the fluorescence of YFP and its donor, cyan fluorescent protein (CFP; FRET ratio), are inversely correlated with intracellular chloride concentration and can be used as a surrogate for interrogating changes in inhibition *in vivo* (Supplementary Fig. 4)[21]. Consistent with the stress-mediated plasticity of inhibitory transmission measured *ex vivo*, footshock stress triggered a rapid and persistent reduction in intracellular chloride in projection neurons of the pPVT, indicating that stress-mediated modulation of inhibition occurs rather rapidly following stress (Fig. 1g, h; Supplementary Fig. 5). Taken together, our results demonstrate that stress is associated with a rapid decrease in $GABA_A$-mediated inhibitory transmission in the pPVT.

Dopamine D2 receptor activation mediates stress-induced plasticity in the pPVT

Next, we investigated the mechanisms controlling stress-induced inhibitory plasticity in the pPVT. Since most projection neurons of the pPVT express D2 receptors (Supplementary Fig. 2), and D2 receptor activation has been previously implicated in the modulation of inhibitory transmission[22–24], we sought to investigate a potential involvement of D2 receptors in the control of inhibitory transmission in the pPVT. Bath application of the D2-like agonist quinpirole triggered a significant reduction in both the amplitude and the frequency of mIPSC recorded from $D2^+$ (but not $D2^-$) neurons of the naïve pPVT (Fig. 2a, b). Because decreases in GABAergic transmission are a core feature of the stressed PVT, we next investigated whether dopaminergic modulation contributed to the effects of stress on inhibition. Consistently, quinpirole-induced inhibitory plasticity was prevented in the pPVT of stressed mice (Fig. 2a, b), suggesting that the effects of stress and quinpirole are mediated by overlapping mechanisms. To evaluate this prediction, we tested the effect of selectively knocking down the expression of the dopamine D2 receptor in the pPVT using a small-hairpin RNA (shRNA) for the *Drd2* gene (AAV-Drd2-shRNA) on stress-induced inhibitory plasticity (Fig. 2c, d). As predicted, restraint-induced inhibitory plasticity was absent only in shRNA expressing neurons of knockdown mice (Fig. 2e–h), indicating that stress-induced inhibitory plasticity requires the function of D2 receptors (although D2-expressing neurons of the pPVT also express low levels of the *Drd3* gene [Supplementary Fig. 6]). Altogether, these results indicate that D2 receptor activation is required for the effects of stress on GABAergic inhibition in the pPVT.

Postsynaptic mechanisms contribute to stress-induced inhibitory plasticity in the pPVT

To investigate if postsynaptic mechanisms contribute to the stress-induced inhibitory plasticity observed in the pPVT, we carried out two separate but complementary approaches. First, we assessed the effect of quinpirole on the postsynaptic response to a fixed volume of GABA directly puffed onto GFP-expressing neurons of *Drd2*-EGFP mice – a manipulation that bypasses presynaptic function (Fig. 3a). Notably, quinpirole elicited a persistent reduction in IPSC amplitude, which was prevented by intracellular infusion of a dynamin inhibitory peptide – a blocker of receptor endocytosis (Fig. 3b, c). Next, two-photon imaging in brain slices of the pPVT revealed a quinpirole-induced decrease in gephyrin puncta in the dendrites of PVT neurons, consistent with the quinpirole-driven internalization of postsynaptic $GABA_A$ receptors (Fig. 3d–f). Taken together, these results suggest that D2-like receptor activation regulates GABAergic inhibition in the pPVT largely through postsynaptic mechanisms.

The LC drives stress-evoked dopamine release in the pPVT

Because we have demonstrated that dopaminergic mechanisms account for stress-induced disinhibition of the pPVT, we used a combination of microdialysis and HPLC to assess whether stress is indeed associated with increases in extracellular dopamine in the pPVT (Fig. 4a, b; Supplementary Fig. 7). Consistently, stress led to a robust and sustained increase in the concentration of dopamine in the pPVT (Fig. 4b), a result that was independently confirmed by mass spectrometry (Brains On-Line, LLC). Furthermore, we observed a stress-mediated delayed increase in the extracellular concentration of two dopamine metabolites (Fig. 4b). This observation is consistent with the robust expression of monoamine oxidase b (*Maob*) in the pPVT (Fig. 4c–d).

The stress-induced dopaminergic modulation of the pPVT is rather surprising, since previous studies have failed to identify a source of dopamine to the midline thalamus and projections from midbrain dopaminergic neurons to the pPVT are negligible[25] (Supplementary Fig. 8). Importantly, however, the locus coeruleus (LC) – which has been recently implicated in dopaminergic modulation of the hippocampus[26,27] – heavily innervates the pPVT (Supplementary Fig. 8; Fig. 4e–g). Interestingly, the distribution of LC afferents to the pPVT is largely restricted to the ventrolateral portion of the pPVT, where $D2^+$ neurons predominate (Fig. 4f). Moreover, upon careful examination of LC afferent inputs to the pPVT using high magnification confocal microscopy, we observed putative synaptic contacts between fluorescently labelled LC terminals and the dendrites of NAc-projecting neurons of the pPVT (Fig. 4g), suggesting that LC terminals may directly innervate projection neurons of the pPVT.

Next, to examine if LC inputs to the pPVT participate in the stress-induced increase in extracellular dopamine, we first performed fiber photometry imaging of GCaMP6s-expressing terminals in the pPVT of dopamine β-hydroxylase-Cre (*Dbh*-Cre)[28] mice expressing GCaMP6s in noradrenergic neurons of the LC (Fig. 4h). This manipulation revealed short latency responses to footshocks (Fig. 4h), indicating that the synaptic inputs from the LC are activated by stress and could be a source of dopamine to the pPVT. However, to directly test this prediction, we combined microdialysis of the pPVT with

chemogenetic silencing of the LC via Cre-dependent expression of the inhibitory *d*esigner *r*eceptor *e*xclusively *a*ctivated by *d*esigner *d*rug (DREADD) hM4Di in the LC of *Dbh*-Cre mice (Fig. 4i). Indeed, chemogenetic silencing of noradrenergic cells of the LC via intraperitoneal (IP) injection of the hM4Di ligand Clozapine-N-Oxide (CNO) prevented the stress-induced increase in extracellular dopamine (Fig. 4j). Interestingly, we noticed that while the effects of stress on extracellular dopamine were prevented in the CNO group, IP administration itself was sufficient to drive a significant increase in extracellular dopamine in both the saline and CNO groups. This result is consistent with the idea that dopamine release in the pPVT is stress dependent and with the known pharmacokinetics of the CNO/DREADD system (stress occurred one hour after the IP injection). Together, these results demonstrate that the LC is responsible for stress-induced dopamine release in the pPVT and suggest that LC inputs to the PVT may be responsible for stress-mediated disinhibition of projection neurons.

Because the LC is primarily a noradrenergic center and increases in norepinephrine (NE) have been previously linked to stressed states[29], we used HPLC to measure the stress-induced changes in NE concentration in the pPVT from the same microdialysis samples gathered during chemogenetic silencing of the LC (same subjects as in Fig. 4j). As expected, stress was associated with a robust increase in the concentration of NE in the pPVT of saline treated mice (Supplementary Fig. 9). However, unlike its effect on stress-induced dopamine, chemogenetic silencing of the LC (CNO treatment) only partially blocked this increase in NE (Supplementary Fig. 9). This result indicates that the LC is only partially responsible for the stress-induced increase in NE concentration in the pPVT, suggesting that the pPVT receives multiple noradrenergic inputs. Indeed, the PVT is densely innervated by two additional noradrenergic centers: the nucleus of the solitary tract and the reticular formation[30] – the latter of which plays a fundamental role in arousal[31]. As a result, whereas the specific cellular effects of NE on neuronal circuits of the pPVT remain intriguing, assessing the role of noradrenergic signaling in the pPVT seemingly implicates multiple sources.

The LC controls inhibitory plasticity in the pPVT

To test the prediction that LC inputs to the pPVT are required for stress-induced inhibitory plasticity, we combined chloride imaging of NAc-projecting pPVT neurons using SuperClomeleon with chemogenetic silencing of the LC via Cre-dependent expression of hM4Di in the LC of *Dbh*-Cre mice (Fig. 5a, b). Animals were exposed to footshock stress on two separate sessions, one in the presence of CNO (day 1) and another one in the presence of saline vehicle (day 2). Given our previous results showing that stress induced inhibitory plasticity persist 24h after stress, CNO and saline treatments were always delivered in this order to prevent learning occurring during the saline session from occluding an effect of stress during a subsequent CNO session (See Fig. 1b–d). As predicted, chemogenetic inhibition of the LC with hM4Di (on day 1) completely prevented the stress-induced changes in intracellular chloride in projection neurons of the pPVT (Fig. 5c–h), demonstrating a role for LC projections to the pPVT in stress-mediated modulation of inhibitory transmission. The opposite effect was observed in the control group, where a stress-induced increase in FRET occurred only on day 1 (CNO treatment; Fig. 5e–h). As

mentioned above, this likely suggests that learning occurring during day 1 prevents an effect of stress on day 2, which is not the case for mice expressing hM4Di in the PVT. Together, these findings exclude a potential effect of CNO on stress-induced modulation of inhibition and demonstrate that LC inputs to the pPVT drive inhibitory plasticity.

The LC controls the stress responsivity of pPVT neurons and enhances aversive learning

To assess the impact of inhibition on the activity of neurons of the pPVT, we first tested the effect of bath application of the non-competitive $GABA_A$ inhibitor picrotoxin (PTX) on the firing rate of $D2^+$ neurons of the pPVT in brain slices. Bath application of PTX elicited a significant increase in the firing rate of $D2^+$ neurons (Supplementary Fig. 10), demonstrating that $GABA_A$-mediated inhibition exerts a strong influence on the excitability of pPVT neurons. Next, to investigate the impact of disinhibition on stress circuits of the pPVT *in vivo*, we used an intersectional approach that allowed restricted expression of the genetically-encoded calcium sensor, GCaMP6s, in NAc-projecting pPVT neurons and assessed stress-evoked fluorescence changes with fiber photometry (Fig. 6a, b). This manipulation revealed that projection neurons of the pPVT are rapidly activated following acute footshock stress (Fig. 6c). Notably, in addition to the fast rise in fluorescence observed shortly after individual footshocks, we reliably detected a steady increase in baseline fluorescence (Fig. 6d). Similar changes in fluorescence were observed when GCaMP6s expression was restricted to $D2^+$ neurons of *Drd2*-Cre mice[28] (Supplementary Fig. 11), consistent with the substantial overlap between $D2^+$ and NAc-projecting neurons of the pPVT (Supplementary Fig. 12). In addition, a subset of mice subjected to tail suspension stress showed similar changes in GCaMP6s fluorescence in projection neurons of the pPVT consistent with the idea that physical and psychological stressors engage largely overlapping circuits in the pPVT (Supplementary Fig. 13; Fig. 1c, d)[3,32]. Importantly, changes in GCaMP6s fluorescence were not correlated with locomotion (Supplementary Fig. 14). Next, we combined GCaMP6s imaging of NAc-projecting pPVT neurons with optogenetic silencing of LC projections to the pPVT of *Dbh*-Cre mice with halorhodopsin (eNphR3.0; Fig. 6e, f). Using this approach, we then compared footshock-evoked pPVT responses between a ‘light ON’ (LC inhibited – on day 1) and a ‘light OFF’ (LC intact – on day 2) test session. Our results demonstrated that optogenetic silencing of LC inputs to the pPVT attenuates the stress-induced increases in baseline fluorescence of pPVT neurons (Fig. 6g–l), suggesting that LC-mediated disinhibition promotes pPVT excitability and amplifies neuronal responses to stress.

Finally, since stress is associated with LC-mediated neurotransmission in the pPVT (Fig. 4–6) and because prior stressful experiences are known to enhance susceptibility to a novel stressor[33] we sought to determine whether LC inputs to the pPVT promote stress susceptibility. For this, we first optogenetically stimulated LC projections to the pPVT of *Dbh*-Cre mice with channelrhodopsin (ChR2; 30 min at 5 Hz) while they navigated an open field. Immediately after, mice were trained with a mild fear conditioning protocol in a novel context (Fig. 7a–c), since the pPVT has been previously shown to participate in fear memory formation[3]. We reasoned that optogenetic stimulation of LC terminals in the pPVT could serve to pre-stress mice thereby increasing their susceptibility to the mild fear conditioning protocol. Remarkably, following conditioning, ChR2-expressing mice displayed a significant

increase in fear memory retrieval (24h later) when compared to the control group (Fig. 7d). Notably, the sensitizing effects of LC terminal stimulation were absent in mice injected with the *Drd2*-shRNA construct in the pPVT (Fig. 7d) and optogenetic stimulation of LC terminals to the pPVT mimicked stress-induced disinhibition *in vitro* (Supplementary Fig. 15). Altogether, these findings demonstrate that LC projections to the pPVT promote stress sensitivity, a result that can be largely attributed to the dopamine-mediated disinhibition of pPVT projection neurons.

DISCUSSION

We have examined the impact of stress on $GABA_A$-mediated inhibitory transmission in the pPVT. Our results demonstrate that stress leads to a robust and persistent disinhibition of projection neurons of the pPVT that requires the activity of postsynaptically-expressed dopamine D2 receptors. Importantly, we conclude that while changes in presynaptic function may contribute to inhibitory plasticity in the pPVT, a D2-driven internalization of $GABA_A$ receptors largely accounts for this phenomenon. Indeed, various observations made here support this conclusion. First, stress was mostly associated with a significant decrease in the amplitude of mIPSCs recorded from $D2^+$ cells of the pPVT. Second, bath application of the D2-like agonist quinpirole triggered a reduction in GABA-mediated responses onto neurons of the pPVT that required dynamin-dependent receptor internalization. Finally, two-photon imaging in brain slices revealed a quinpirole-induced decrease in the density of gephyrin puncta in dendrites of neurons of the pPVT[34–36]. Altogether, our findings highlight dopaminergic transmission as an important modulator of PVT function and identify the LC as both a major source of dopamine to the pPVT and a driver of disinhibition. These findings provide the first evidence of a stress-mediated circuit mechanism that drives disinhibition in the midline thalamus. Future studies should focus on investigating the precise molecular mechanism by which D2 receptor activation leads to $GABA_A$ receptor internalization.

Like other midline and intralaminar nuclei of the rodent thalamus, the pPVT virtually lacks GABAergic interneurons[7]. Instead, the pPVT receives dense inhibitory projections from several extrathalamic nuclei that span the basal forebrain, the hypothalamus, the midbrain, and the pons. Such profoundly diverse innervation of the pPVT suggests that inhibition exerts a tight control on the excitability of projection neurons within the midline thalamus[13]. This idea is supported by our observation that pharmacological blockade of $GABA_A$ receptors significantly increased the firing rate of neurons of the pPVT. As such, stress-induced disinhibition of the pPVT can lead to an increased recruitment of projection neurons. Indeed, increased activation of the PVT has been widely associated with aversive states[5,6,37]. To this end, the postsynaptic locus of inhibitory plasticity we uncovered may serve to decrease the PVT's sensitivity to inhibitory inputs and promote stressed states.

The source of dopamine to the PVT has remained a matter of debate for nearly three decades[25,38] with previous studies suggesting the hypothalamus and periaqueductal gray as unlikely-yet-possible candidates[25]. Indeed, despite its robust expression of dopaminergic markers, the PVT receives little to no innervation by midbrain dopaminergic neurons[25]. Instead, here, we have demonstrated that the LC is a major source of dopamine to the pPVT. Our results are consistent with recent reports regarding dopaminergic actions of LC input to

the hippocampus[26,27] and suggest that LC-mediated dopamine may be a widespread phenomenon. Future studies would be required to disentangle the precise neurochemical footprint of LC inputs across its different target structures. However, it is important to highlight that a detailed evaluation of the dopaminergic effects of LC innervation, as well as the potential co-release of dopamine and norepinephrine from LC terminals, would require the development of new molecular and/or imaging tools that allow for the unequivocal identification of both neurotransmitters with high spatial and temporal resolution.

By enhancing neuronal excitability in the pPVT through disinhibitory mechanisms, the LC could facilitate recruitment of the PVT during stress and promote the formation of aversive memory. Similarly, stress-induced disinhibition of the pPVT may serve to sensitize subjects to novel stressors. Our finding that pre-stimulation of LC input to the pPVT enhances subsequent fear conditioning in a D2-dependent manner is consistent with this idea. Importantly, while we did not assess whether LC-pPVT stimulation alone was sufficient to fear condition subjects, this possibility seems unlikely in light of a recent publication by Uematsu and colleagues[39]. In this study, the authors demonstrated that while optogenetic stimulation of LC projections to the amygdala enhances fear conditioning, stimulation of these projections alone (in the absence of a footshock) was not sufficient to drive conditioning[39]. Our results are consistent with an overall role for the LC in promoting aversive states and stress sensitivity. Moreover, these observations agree with a well-documented role for the LC in the processing of salient events through the recruitment of arousal, attention, and memory circuits[40]. It is worth noting that inhibition of the LC did not prevent the stress-induced activation of the pPVT, but instead led to a significant attenuation of stress-induced calcium responses, suggesting a gain control role for LC inputs to the pPVT. A similar gain control mechanism was recently proposed for LC projections to the auditory cortex[41]. Altogether, our study provides the first evidence of how neurotransmitter systems are integrated in the PVT to shape its overall function.

It is important to highlight that while the PVT has been linked to the emergence of adaptive behavioral responses to stress[25], the cellular and circuit mechanisms by which this stress-mediated recruitment of the PVT promotes adaptive responding remain unknown. One possibility is that the PVT drives the selection of specific adaptive behaviors via its projections to limbic areas such as the NAc and the amygdala. However, this scenario seems unlikely because 1) PVT projections to its downstream targets are relatively weak[3] (but see Zhu and colleagues[5]), and 2) different stressors appear to activate overlapping subpopulations of PVT neurons and lead to similar plastic changes as shown here. Instead, the PVT likely exerts a modulatory role onto its downstream targets through the enhancement of neuronal excitability. This in turn may facilitate the recruitment of neuronal networks in target regions and invigorate stress-coping actions. Notably, we recently showed that in fear conditioned animals, PVT projections promote the excitability of a defined class of neurons within the central nucleus of the amygdala that encode fear memory[3]. Such modulatory actions of the pPVT may be conserved across its various limbic targets and potentially serve to promote motivated responding. Notably, the neighboring mediodorsal thalamus has been recently demonstrated to exert a modulatory role in the prefrontal cortex where it helps sustain ongoing representation during an attention task and does so in a

categorically-free manner[42]. The idea that the PVT may elicit similar categorically-free modulatory actions over limbic areas is an enticing possibility.

A major view of the functional organization of the thalamus classifies inputs to projection neurons as either 'drivers' or 'modulators', with the source of 'driver' input to the various thalamic nuclei being the major determinant in their designation as either 'first order' (receiving subcortical driver input) or 'higher order' (receiving driver input from layer 5 of the cortex) relays[43]. Thus, whereas the lateral geniculate nucleus contains first order relays, the mediodorsal nucleus is primarily populated with higher order relays. The overall classification of thalamic relays as either first or higher order is largely due to a detailed anatomical and functional characterization of afferent inputs to the various thalamic nuclei[44]. This, however, is not the case for the midline thalamus for which identification of either first or higher order relay is currently lacking. Proper classification of PVT projection neurons will require in depth analysis of both driver and modulator inputs. Therefore, by identifying the LC as a major modulator input to the PVT, our work contributes vital information towards a better conceptualization of the functional organization of this thalamic structure.

METHODS

Mice

All procedures were performed in accordance with the *Guide for the Care and Use of Laboratory Animals* and were approved by the National Institute of Mental Health Animal Care and Use Committee. Mice used in this study were housed under a 12-h light-dark cycle (6 a.m. to 6 p.m. light), with food and water available *ad libitum*. The following mouse lines were used: *Drd2*-EGFP (GENSAT – founder line S1118), *Drd2*-Cre (GENSAT – founder line ER44), *Dbh*-Cre (GENSAT – founder line KH212) and *Ai14 (The Jackson Laboratory)*. In addition, we used C57BL/6NJ strain mice (The Jackson Laboratory). Both male and female mice 7–12 weeks of age were used for all experiments. Animals were randomly allocated to the different experimental conditions reported in this study.

Viral vectors

AAV9-Syn-Flex-GCaMP6s-WPRE-SV40 and was produced by the Vector Core of the University of Pennsylvania. AA9-CAG-FLEX-tdTomato was produced by the Vector Core of the University of North Carolina. AAV9-CMV-DIO-Cerulean-deltaC11-WPRE-SV40 (a.ka. AAV9-CMV-DIO-SuperClomeleon or SuperClomeleon) was produced by Virovek, Inc. from plasmid kindly provided by Dr. George Augustine (Lee Kong Chian School of Medicine, Singapore). AAV2-hSyn-DIO-hM4Di-mCherry was produced by Addgene. AAV9-GFP-U6-mDRD2-shRNA and AAV2(retro)-CAG-iCre (Addgene plasmid # 81070) were produced by Vector Biolabs. All viral vectors were stored in aliquots at −80°C until use.

Drugs

All drugs used in this study where purchased from Tocris (PTX, catalog# 1128; NBQX, catalog# 1044; D-APV, catalog# 0106; TTX, catalog# 1078; quinpirole, catalog# 1061;

sulpiride, catalog# 0895; 4-AP, catalog# 0940), with the exception of CNO which was purchased from Enzo Life Sciences (catalog# BML-NS105).

Stereotaxic surgery

All viral injections were performed using previously described procedures[4] and an AngleTwo stereotaxic device (Leica Biosystems) at the following stereotaxic coordinates: pPVT, −1.60 mm from Bregma, 0.06 mm lateral from midline, and −3.30 mm vertical from cortical surface; NAc, 1.70 mm from Bregma, 0.60 mm lateral from midline, and −4.54 mm vertical from cortical surface; LC, −5.50 mm from Bregma, 0.95 mm lateral from midline, and −3.90 mm vertical from cortical surface. For fiber photometry imaging and optogenetic experiments, an optical fiber (400 μm for photometry, 200 μm for optogenetics) (Doric Lenses) was implanted over the pPVT immediately after viral injections (coordinate: –1.60 mm from Bregma, 0.05 mm lateral from midline, and −2.90 mm vertical from cortical surface) and cemented using Metabond Cement System (Parkell, Inc.) and Jet Brand dental acrylic (Lang Dental Manufacturing Co., Inc.). Following all surgical procedures, animals recovered on a heating pad and returned to their home cages after 24 h post-surgery recovery and monitoring. Animals received subcutaneous injections with metacam (meloxicam, 1–2 mg/kg) for analgesia and anti-inflammatory purposes. All AAVs were injected at a total volume of approximately 1 μl and were allowed 2–3 weeks for maximal expression. For retrograde tracing of NAc-projecting pPVT cells, CTB-647 or CTB-555 (0.5–0.6 μl, 1.0% in PBS) (ThermoFisher Scientifc) was injected into the shell of the NAc and allowed 3–5 days for retrograde transport. Mice without correct targeting of tracers and/or vectors were excluded from this study.

Histology

Animals were deeply anesthetized with euthanasia solution and transcardially perfused with PBS, followed by paraformaldehyde (PFA; 4% in PBS). After extraction, brains were postfixed in 4% PFA at 4 °C for at least 2 hours, and subsequently transferred to a 30% PBS-buffered sucrose solution for cryoprotection until brains were saturated (~24–36 h). Coronal brain sections (45 μm) were cut using a freezing microtome (SM 2010R, Leica). Brain sections were blocked in 10% normal goat serum (NGS) in PBST (0.1% Triton X-100 in PBS) for 1 hr at RT, followed by incubation with primary antibodies in 10% NGS-PBST overnight at 4 °C. Sections were then washed with PBST (5 × 15 min) and incubated with fluorescent secondary antibodies at RT for 1 h. All washes and incubations were done over a shaker at low speed. After washing with PBS (5 × 15 min), sections were mounted onto glass slides with Fluoromount-G (Beckman Coulter). Images were taken using a LSM 780 laser-scanning confocal microscope (Carl Zeiss). Image analysis and cell counting were performed using ImageJ software. For shRNA experiments, knockdown efficiency was determined by first calculating the corrected total fluorescence (CTF) for a 50 × 50 pixel window from both an AAV infected and a non-infected portion of the pPVT. Next, the background CTF (a fixed region outside PVT) was subtracted from both the infected (I_true) and non-infected (NI_true) CTF. Finally, percentage of knockdown was estimated using the following equation: (NI_true – I_true/NI_true) × 100.

Antibodies

The primary antibodies used were: anti-GFP (1:1000, chicken, Abcam, catalog# ab13970, lot# GR236651-24); anti-TH (1:1000, rabbit, Immunostar, catalog# 22941, lot# 1552001); and anti-mCherry (1:1000, mouse, Living Colors/Clontech, catalog# 632543, lot# 1506199A). Fluorophore-conjugated secondary antibodies were purchased from ThermoFisher Scientific. Specifically, the following secondary antibodies were used in this study: goat anti-rabbit-488 (1:500, catalog# A11034, lot# 1737902), goat anti-chicken-488 (1:500, catalog# A11039, lot# 1759025) and goat anti-mouse (1:500, catalog# A11004, lot# 1698376). Antibodies were diluted in PBS with 10% NGS and PBST. Additional validation details are available from the manufacturer for each antibody used in this study.

Electrophysiology

For electrophysiological experiments, mice were anaesthetized with isoflurane, decapitated and their brains quickly removed and chilled in ice-cold dissection buffer (110.0 mM choline chloride, 25.0 mM $NaHCO_3$, 1.25 mM NaH_2PO_4, 2.5 mM KCl, 0.5 mM $CaCl_2$, 7.0 mM $MgCl_2$, 25.0 mM glucose, 11.6 mM ascorbic acid and 3.1mM pyruvic acid, gassed with 95% O_2 and 5% CO_2). Coronal sections (300 μm thick) containing the pPVT were cut in dissection buffer using a VT1200S automated vibrating-blade microtome (Leica Biosystems), and were subsequently transferred to incubation chamber containing artificial cerebrospinal fluid (ACSF) (118 mM NaCl, 2.5 mM KCl, 26.2 mM $NaHCO_3$, 1 mM NaH_2PO_4, 20 mM glucose, 2 mM $MgCl_2$ and 2 mM $CaCl_2$, at 34 °C, pH 7.4, gassed with 95% O_2 and 5% CO_2). After at least 40 min recovery time, slices were transferred to room temperature (20–24 °C) and were constantly perfused with ACSF.

For synaptic plasticity experiments, recordings were always performed on interleaved naïve and stressed animals. Whole-cell patch-clamp recordings from pPVT neurons were obtained with Multiclamp 700B amplifiers (Molecular Devices), under visual guidance with an Olympus BX51 microscope with transmitted light illumination. $D2^+$ pPVT neurons were identified based on their fluorescence (eGFP or tdTomato). Recordings were made at holding potentials of −70 mV using a high chloride internal solution (130 mM CsCl, 1mM $MgCl_2$, 10 mM HEPES, 0.1 mM EGTA, 4 mM NaCl, 4 mM Na_2-ATP, 0.3 mM Na_3-GTP, 10 mM, 5 mM QX-314 (pH 7.2) and low-pass filter (1 KHz). mIPSCs were recorded in the presence of tetrodotoxin (TTX; 1 μM), NBQX (20 μM) and D-APV (50 μM) and analyzed using Mini Analysis software (Synaptosoft).

To elicit $GABA_A$ receptor-mediated responses in pPVT neurons, GABA (1 μM) was puffed over recorded $D2^+$ pPVT neurons using a blunt patch pipette placed in close proximity to the recorded neuron (<20 μm) in the presence of TTX (1 μM), NBQx (20 μM), and D-APV (50 μM).

Fiber photometry-based optical calcium measurements

Mice were first allowed to adapt to the experimental cages and fiber patchcord for at least 15 min prior to each testing session. To record fluorescence signals, the fiber photometry system (Doric Lenses) used two continuous sinusoidally modulated LED (DC4100, ThorLabs) at 473 nm (211 Hz) and 405 nm (531 Hz) that served as light source to excite

GCaMP6s and an isosbestic autofluorescence signal respectively. Both lights were coupled to a large core (400 μm), high NA (0.48) optical fiber patchcord, which was mated to a matching brain implant in each mouse. The light intensity at the interface between the fiber tip and the animal ranged from 10–15 μW (but was constant throughout each testing session). GCaMP6s and autofluorescence signals were collected by the same fiber, and focused onto two separate photoreceivers (2151, Newport Corporation). An RZ5P acquisition system (Tucker-Davis Technologies; TDT), equipped with a real-time signal processor controlled the LEDs and also independently demodulated the fluorescence brightness due to 473 nm and 405 nm excitation. The occurrence of behavioral manipulations was recorded by the same system via TTL input. Data was analyzed by first applying a least-squares linear fit to the 405 nm signal to align it to the 470 nm signal. The resulting fitted 405 nm signal was then used to normalize the 473 nm as follows: $\Delta F/F$ = (473 nm signal – fitted 405 nm signal)/fitted 405 nm signal. Changes in baseline fluorescence after stress were determined by comparing the last 30 s of imaging data to the 30 s prior to the onset of stress.

All experiments were performed in behavioral chambers (Coulbourn Instruments) and video recorded using video cameras installed above each behavioral chamber. Behavioral variables, such as shocks and tail suspensions, were marked in the signaling traces via the real-time processors as TTL signals from Coulbourn Instruments software. This allowed for exact temporal profile of calcium fluorescence signals in the pPVT as a response to stressors. Analysis of the effect of restraint stress on calcium and chloride changes in neurons of the pPVT was omitted due to technical limitations.

Fiber photometry-based optical chloride measurements

A modified optical fiber photometry apparatus was used to measure bulk changes in intracellular chloride concentrations as a surrogate for synaptic inhibition. For this, a viral construct coding for SuperClomeleon (described above) was expressed in NAc-projecting neurons of the pPVT. SuperClomeleon is a fluorescence resonance energy transfer (FRET) chloride sensor comprised of a cyan fluorescent protein (CFP; FRET donor) fused to a yellow fluorescent protein (YFP; FRET acceptor), which contains a chloride binding site. Chloride binding to YFP quenches its fluorescence emission, as such, under conditions of reduced chloride concentrations the FRET ratio increases. For fluorescence signals detection, the procedures used for fiber implant and the fiber-photometry system were identical as those used for the *in vivo* calcium imaging (see above), with the exception of the light emission wavelength and the filters used to excite and collect both CFP and YFP emission. To excite CFP, a continuous LED at 425 nm light was used. As described above, light was delivered and collected through the same optic fibers via a custom built light cube (Doric Lenses). CFP (465 nm) and YFP (535 nm) emissions were separated using a single-edge beam splitter and focused independently onto two separate photoreceivers (2151, Newport Corporation). Fluorescence signals were digitized and recorded using the RZ5P acquisition system, as described above.

Analysis of the bulk changes in intracellular chloride concentrations was performed as follows: the FRET ratio was calculated as CFP / YFP across all time points during the

recording period. Changes in baseline FRET ratio after stress were determined by comparing the last 30 s of imaging data to the 30 s prior to the onset of stress.

Stress behavioral protocols

Footshocks—Following habituation to the behavioral chamber, mice received five presentations of a 2-s 1mA unsignaled footshock. The behavioral chamber was illuminated throughout the entire procedure. For electrophysiological experiments, mice were returned to their home cages for 2 h and subsequently sacrificed (see above). For optogenetics (halorhodopsin) and chemogenetics (DREADD) experiments, animals were stressed over two individual sessions. Light ON and CNO sessions occurred on day 1, whereas Light OFF and Saline sessions occurred on day 2. This order was established in order to prevent learning during the Light OFF and Saline session from occluding an effect of optogenetic and chemogenetic manipulations.

Tail suspensions—Animals where tethered to an optical patchcord and allowed to habituate for 15 minutes. After this, animals were suspended by their tails by a single experimenter for total of five occurrences, each lasting 10–12 s every two minutes. Calcium signals were detected as described above.

Restraint stress for electrophysiological recordings—Mice were handled for three consecutive days, and subsequently subjected to a 2 h restraint stress. The restraint procedure consisted of inserting individual animals into a decapicone (Braintree Scientific). Subjects were secured inside the decapicone by a tape wrapped around the base of their tails. Animals were constantly monitored to ensure proper ventilation.

Optogenetic enhancement of mild fear conditioning

Mice injected with either Cre-dependent ChR2 or Cre-dependent tdTomato (control) in the LC were behaviorally tested three weeks later. First, mice were tethered with an optical patch cord and placed in an open field box (45 cm × 45 cm × 40 cm) where they received light stimulation with a blue laser (473 nm) at a frequency of 5 Hz for 30 min. A similar protocol has been shown to produce responses that mimic those evoked by stress[45–47]. Immediately after, mice were fear conditioned in a Mouse Test Cage (18 cm × 18 cm × 30 cm). The Test Cage was located inside a sound attenuated cabinet (H10-24A; Coulbourn Instruments, Whitehall, PA) and equipped with an electrified floor connected to a shock generator (H13-15; Coulbourn Instruments). During both conditioning and the subsequent test of contextual memory, the cabinet was illuminated and the behavior captured with a USB camera (ACT-VP-02; Coulbourn Instruments) at 3.7 Hz and stored on a personal computer. The FreezeFrame software (Coulbourn Instruments) was used to control the delivery of footshocks. During conditioning (day 1), mice received five 0.4-mA footshocks (each footshock lasted 2 s). A test for contextual fear memory was performed 24 h following conditioning (day 2) by returning mice to the conditioning context for 5 min. Freezing behavior was recorded and analyzed for the entire 5 min with FreezeFrame (Coulbourn Instruments).

Two-photon imaging of putative GABAergic synapses

Stereotactic viral injection—Surgeries were performed on 4–6 week-old mice. The cocktail of ketamine (0.1 mg/g) and xylazine (0.01 mg/g) (Sigma-Aldrich) was used to anesthetize mice via intraperitoneal injection. Hair was removed and the head was fixed to stereotactic device (Kopf instruments, Tujunga, CA, USA) by ear bars and a nose clamp. During surgery, body temperature was maintained constantly at 37°C using a homeothermic blanket with flexible probe (Harvard Apparatus, Holliston, MA, USA). Head skin was carefully removed by a sharp surgical scissor and scalpel. Small burr hole (~0.5 mm in diameter) was made by a hand-held drill (Fordom Electric Co., Bethel, CT, USA) under the surgical microscope. In order to target paraventricular nucleus of the thalamus (PVT), 300–450 nl of viral stock solution (AAV1-CAG-Flex-TdTomato-WPRE-bGH: AAV1-CAG-Flex-Teal-gephyrin: AAV1-CMV-PI-Cre-rBG = 5: 5: 0.2) was injected to the ventral portion of posterior PVT (Coordinates: AP, −1.60 mm; ML, +0.06 mm from bregma, and DV −3.30 mm from the brain surface) using micropipette (speed: 100~200 nl/min). After injection, micropipette was held for 3 minutes to prevent backflow of viral solutions.

Slice preparation—5–9 weeks after viral injection, the mice were deeply anesthetized with isoflurane and they were decapitated. The brain was quickly removed and chilled in ice-cold high-magnesium cutting solution containing the followings (in mM): 100 Choline Chloride, 25 $NaHCO_3$, 2.5 KCl, 0.5 $CaCl_2$, 7 $MgCl_2$, 1.25 NaH_2PO_4, 25 glucose, 20 HEPES, 3.1 Na-pyruvate, 5 Na-ascorbate. pH and osmolarity were adjusted to 7.4 and ~300 mOsm, respectively. The isolated brain was placed onto the stage of a vibratome (Leica VT1000, Leica Biosystems, Buffalo Grove, IL, USA) and 300 μm-thick coronal slices were cut. The slices were transferred and incubated at 34°C for 30 min in a slice container superfused with artificial cerebrospinal fluid (ACSF) solution containing the followings (in mM): 124 NaCl, 26 $NaHCO_3$, 3.2 KCl, 2.5 $CaCl_2$, 1.3 $MgCl_2$, 1.25 NaH_2PO_4, 10 glucose, saturated with 95% O_2 and 5% CO_2 gas. Thereafter slices were maintained at room temperature for the experiments.

Two-photon slice imaging—The PVT neurons from the acute slice were imaged in ACSF using a two-photon microscopy (Prairie Technologies, Inc). For each neuron, image stacks (512 × 512 pixels; 0.048 μm / pixel) with 1-μm z-steps were collected from one segment of apical dendrites at the wavelength of 920 nm (Mai Tai DeepSee, Spectra Physics). All images shown are maximum projections of 3D image stacks after applying a median filter (2 × 2) to the raw image data.

Quantification of fluorescence intensities of Teal-gephyrin puncta—Teal-gephyrin fluorescence intensities were calculated from bleed-through-corrected and background-subtracted green (Teal-gephyrin) fluorescence intensities using the integrated pixel intensity of a boxed region surrounding a Teal-gephyrin punctum, as previously described (Oh et al., 2016). In brief, Teal-gephyrin puncta whose green fluorescence intensities were higher than two standard deviations (2 SDs) of the local background green fluorescence levels measured from 2 ROIs near the puncta were recognized as true Teal-gephyrin puncta and counted in images from the green channel using ImageJ. The G/R (G:

Teal-gephyrin, R: TdTomato) value of individual gephyrin punctum was analyzed using ImageJ (NIH).

Microdialysis and HPLC

Extracellular dopamine (DA), and metabolites 3,4-dihydroxyphenylacetic acid (DOPAC) and homovanillic acid (HVA) were measured from PVT by microdialysis coupled to HPLC with electrochemical detection as previously described[48]. Briefly, a 6 mm-long 21-gauge guide cannula was chronically implanted in PVT (AP: −1.6mm, L: 2.4mm, V: 1.9mm, angle 35°) in adult (~3 month) wild-type C57BL/6J mice and a week later, a microdialysis probe (1 mm-long, 18 kDA MW cutoff) was lowered through the guide cannula to collect twelve consecutives 10 min-long (1 μl/min flow rate) samples in modified cerebrospinal fluid (ACSF) (136mM NaCl, 3.7mM KCl, 2.2mM $CaCl_2$, 1mM $MgCl_2$, and 10mM $NaHCO_3$ at pH 7.4). Samples were immediately injected into an isocratic HPLC system coupled to electrochemical detection (LC-4A, BASi; West Lafayette, IN) for measurements of DA, DOPAC and HVA levels. We estimated the *in vitro* DA, DOPAC and HVA percentage of recovery for each microdialysis probe and concentration corrected for each experiment. DA, DOPAC and HVA were measured by comparing the area under the curve (AUC) of the samples vs. the AUC of standard curve and corrected with respect to the percentage of recovery from the dialysis probe for each molecule. Detection limit at 1 nA of sensitivity for DA, DOPAC and HVA were estimated in 2.5, 2.4, 1.3 and 2.7 pg respectively by building up a calibration curve for each molecule. After microdialysis experiments, probe placement was identified by Nissl staining histological analysis. Brains with probe tracks outside the PVT were excluded from analysis. Dopamine detection with microdialysis was independently confirmed by mass spectrometry (Brains Online; California, USA).

In Situ Hybridization

In situ hybridization (ISH) was performed by using ViewRNA™ ISH Tissue two-plex assay (Affymetrix). Briefly, fresh brains were dissected and frozen on dry ice immediately. Next, brain sections containing the PVT were prepared with a cryostat (18 μm) and mounted glass slide and fixed with 4% formaldehyde overnight. The next day, slides were dehydrated in 50%, 70%, and finally 100% ethanol for 10 minutes each. After 30 min heating at 60°C, slices were incubated with protease enzyme for 10 min at 40°C, and then washed with PBS. The following procedures were performed orderly and sections were washed with PBS between each step: At 40°C, slices were incubated with MAOB, D2 and/or D3 probe for two hours, PreAmplifier Mix for 25 min, Amplifier Mix QT for 15 min, label probe 1-AP for 15 min, AP enhancer solution for 5 min, fast red substrate for 30 min (fast blue for probe 2-AP), and then counterstain with DAPI for 2 min at room temperature. Images were acquired using a Zeiss LSM780 confocal microscope.

Quantitative Polymerase Chain Real-Time Reaction (qPCR)

Total RNA from dissected midline thalamus and cortex were obtained by using the RNeasy Lipid Tissue Mini kit (QIAGEN). Each purified RNA sample (4 μg) was reverse-transcribed into cDNA using a High Capacity cDNA Archive kit (Thermo Fisher Scientific). The reaction was performed at 25°C for 10 min, 37°C for 120 min, and 85°C for 5 min. We used Fast Start Universal Probe master mix (Roche Applied Science) qPCR reaction and

monoamine oxidase B (MAOB) gene expression assays (Integrated DNA Technologies). Negative controls with absence of reverse transcriptase were comprised in each assay. qPCR reactions were activated at 95°C for 10 min, and then 40 cycles of 95°C for 15 seconds and 60°C for 1 min. mRNA expression levels were calculated by using the $2^{-\Delta\Delta Ct}$ method, where C_t=cycle threshold number, ΔC_t=β-actin C_t–target gene C_t, $\Delta\Delta C_t$=ΔC_t control–ΔC_t restrain, and the MAOB mRNA levels from PVT were quantified relative to MAOB mRNA levels from cortex with β-actin as the internal reference.

Statistics and data presentation

All data were imported to OriginPro (OriginLab Corp.) for statistical analyses. Initially, normality tests (D'Agostino-Pearson and Kolmogorov-Smirnov) were performed to determine the appropriate of the statistical tests used. All data are presented as mean ± s.e.m. No assumptions or corrections were made prior to data analysis. Differences between two groups were always examined using a two-sided Student's t-test, where $P<0.05$ was considered significant and $P>0.05$ was considered non-significant. Comparisons between multiple groups were performed using ANOVA (one-way and two-way), followed by Tukey's test. All cell counting experiments and behavioral testing were performed by an experimenter blind to the experimental condition. For all other experiments data collection and analysis were not performed blind to the conditions of the experiments. The sample sizes used in our study, such as the numbers of neurons or animals, are about the same or exceed those estimated by power analysis (power = 0.9, $\alpha = 0.05$). For electrophysiological analyses, the sample size is 9–32 cells, depending on the specific aim of the experiment (e.g. pharmacology vs experience-dependent plasticity). For fiber photometry analyses, the sample size is 4–9 mice. For morphological and immunohistochemical analyses, the sample size is 2–11 mice. For fear conditioning the sample size is 7 mice per group. All experiments were replicated at least once.

Life Sciences Reporting Summary

Additional information on experimental design and materials used in our study is available in the Life Sciences Reporting Summary.

Data availability

All the data that support the findings presented in this study are available from the corresponding author upon reasonable request.

Supplementary Material

Refer to Web version on PubMed Central for supplementary material.

Acknowledgments

This work was supported by the NIMH Intramural Research Program (M.A.P.), NICHD Intramural Research Program (A.B.) and NIH Grant MH107460 (H.B.K.). We thank Thomas Davidson for his assistance in the design of the fiber photometry system.

References

1. Vertes RP, Linley SB, Hoover WB. Limbic circuitry of the midline thalamus. Neurosci Biobehav Rev. 2015; 54:89–107. DOI: 10.1016/j.neubiorev.2015.01.014 [PubMed: 25616182]
2. Hsu DT, Kirouac GJ, Zubieta JK, Bhatnagar S. Contributions of the paraventricular thalamic nucleus in the regulation of stress, motivation, and mood. Front Behav Neurosci. 2014; 8:73. [PubMed: 24653686]
3. Penzo MA, et al. The paraventricular thalamus controls a central amygdala fear circuit. Nature. 2015; 519:455–459. DOI: 10.1038/nature13978 [PubMed: 25600269]
4. Do-Monte FH, Quinones-Laracuente K, Quirk GJ. A temporal shift in the circuits mediating retrieval of fear memory. Nature. 2015; 519:460–463. DOI: 10.1038/nature14030 [PubMed: 25600268]
5. Zhu Y, Wienecke CF, Nachtrab G, Chen X. A thalamic input to the nucleus accumbens mediates opiate dependence. Nature. 2016; 530:219–222. DOI: 10.1038/nature16954 [PubMed: 26840481]
6. Do-Monte FH, Minier-Toribio A, Quinones-Laracuente K, Medina-Colon EM, Quirk GJ. Thalamic Regulation of Sucrose Seeking during Unexpected Reward Omission. Neuron. 2017; 94:388–400 e384. DOI: 10.1016/j.neuron.2017.03.036 [PubMed: 28426970]
7. Arcelli P, Frassoni C, Regondi MC, De Biasi S, Spreafico R. GABAergic neurons in mammalian thalamus: a marker of thalamic complexity? Brain Res Bull. 1997; 42:27–37. [PubMed: 8978932]
8. Zhang X, van den Pol AN. Rapid binge-like eating and body weight gain driven by zona incerta GABA neuron activation. Science. 2017; 356:853–859. DOI: 10.1126/science.aam7100 [PubMed: 28546212]
9. Betley JN, Cao ZF, Ritola KD, Sternson SM. Parallel, redundant circuit organization for homeostatic control of feeding behavior. Cell. 2013; 155:1337–1350. DOI: 10.1016/j.cell.2013.11.002 [PubMed: 24315102]
10. Giber K, et al. A subcortical inhibitory signal for behavioral arrest in the thalamus. Nat Neurosci. 2015; 18:562–568. DOI: 10.1038/nn.3951 [PubMed: 25706472]
11. Bodor AL, Giber K, Rovo Z, Ulbert I, Acsady L. Structural correlates of efficient GABAergic transmission in the basal ganglia-thalamus pathway. J Neurosci. 2008; 28:3090–3102. DOI: 10.1523/JNEUROSCI.5266-07.2008 [PubMed: 18354012]
12. Wanaverbecq N, et al. Contrasting the functional properties of GABAergic axon terminals with single and multiple synapses in the thalamus. J Neurosci. 2008; 28:11848–11861. DOI: 10.1523/JNEUROSCI.3183-08.2008 [PubMed: 19005050]
13. Halassa MM, Acsady L. Thalamic Inhibition: Diverse Sources, Diverse Scales. Trends Neurosci. 2016; 39:680–693. DOI: 10.1016/j.tins.2016.08.001 [PubMed: 27589879]
14. Del Castillo J, Katz B. Quantal components of the end-plate potential. J Physiol. 1954; 124:560–573. [PubMed: 13175199]
15. Redman S. Quantal analysis of synaptic potentials in neurons of the central nervous system. Physiol Rev. 1990; 70:165–198. [PubMed: 2404288]
16. Stevens CF. Quantal release of neurotransmitter and long-term potentiation. Cell. 1993; 72(Suppl): 55–63. [PubMed: 8094037]
17. Goldstein JM, Jerram M, Abbs B, Whitfield-Gabrieli S, Makris N. Sex differences in stress response circuitry activation dependent on female hormonal cycle. J Neurosci. 2010; 30:431–438. DOI: 10.1523/JNEUROSCI.3021-09.2010 [PubMed: 20071507]
18. Ramikie TS, Ressler KJ. Mechanisms of Sex Differences in Fear and Posttraumatic Stress Disorder. Biol Psychiatry. 2017
19. Grimley JS, et al. Visualization of synaptic inhibition with an optogenetic sensor developed by cell-free protein engineering automation. J Neurosci. 2013; 33:16297–16309. DOI: 10.1523/JNEUROSCI.4616-11.2013 [PubMed: 24107961]
20. Dong X, Li S, Kirouac GJ. Collateralization of projections from the paraventricular nucleus of the thalamus to the nucleus accumbens, bed nucleus of the stria terminalis, and central nucleus of the amygdala. Brain Struct Funct. 2017; 222:3927–3943. DOI: 10.1007/s00429-017-1445-8 [PubMed: 28528379]

21. Wimmer RD, et al. Thalamic control of sensory selection in divided attention. Nature. 2015; 526:705–709. DOI: 10.1038/nature15398 [PubMed: 26503050]
22. Dobbs LK, et al. Dopamine Regulation of Lateral Inhibition between Striatal Neurons Gates the Stimulant Actions of Cocaine. Neuron. 2016; 90:1100–1113. DOI: 10.1016/j.neuron.2016.04.031 [PubMed: 27181061]
23. Floran B, Floran L, Sierra A, Aceves J. D2 receptor-mediated inhibition of GABA release by endogenous dopamine in the rat globus pallidus. Neurosci Lett. 1997; 237:1–4. [PubMed: 9406865]
24. Lalchandani RR, van der Goes MS, Partridge JG, Vicini S. Dopamine D2 receptors regulate collateral inhibition between striatal medium spiny neurons. J Neurosci. 2013; 33:14075–14086. DOI: 10.1523/JNEUROSCI.0692-13.2013 [PubMed: 23986243]
25. Li S, Shi Y, Kirouac GJ. The hypothalamus and periaqueductal gray are the sources of dopamine fibers in the paraventricular nucleus of the thalamus in the rat. Front Neuroanat. 2014; 8:136. [PubMed: 25477789]
26. Kempadoo KA, Mosharov EV, Choi SJ, Sulzer D, Kandel ER. Dopamine release from the locus coeruleus to the dorsal hippocampus promotes spatial learning and memory. Proc Natl Acad Sci U S A. 2016; 113:14835–14840. DOI: 10.1073/pnas.1616515114 [PubMed: 27930324]
27. Takeuchi T, et al. Locus coeruleus and dopaminergic consolidation of everyday memory. Nature. 2016; 537:357–362. DOI: 10.1038/nature19325 [PubMed: 27602521]
28. Gerfen CR, Paletzki R, Heintz N. GENSAT BAC cre-recombinase driver lines to study the functional organization of cerebral cortical and basal ganglia circuits. Neuron. 2013; 80:1368–1383. DOI: 10.1016/j.neuron.2013.10.016 [PubMed: 24360541]
29. Abercrombie ED, Keller RW Jr, Zigmond MJ. Characterization of hippocampal norepinephrine release as measured by microdialysis perfusion: pharmacological and behavioral studies. Neuroscience. 1988; 27:897–904. [PubMed: 3252176]
30. Kirouac GJ. Placing the paraventricular nucleus of the thalamus within the brain circuits that control behavior. Neurosci Biobehav Rev. 2015; 56:315–329. DOI: 10.1016/j.neubiorev.2015.08.005 [PubMed: 26255593]
31. Moruzzi G, Magoun HW. Brain stem reticular formation and activation of the EEG. Electroencephalogr Clin Neurophysiol. 1949; 1:455–473. [PubMed: 18421835]
32. Cullinan WE, Herman JP, Battaglia DF, Akil H, Watson SJ. Pattern and time course of immediate early gene expression in rat brain following acute stress. Neuroscience. 1995; 64:477–505. [PubMed: 7700534]
33. Dallman MF, et al. Chronic stress-induced effects of corticosterone on brain: direct and indirect. Ann N Y Acad Sci. 2004; 1018:141–150. DOI: 10.1196/annals.1296.017 [PubMed: 15240363]
34. Oh WC, Lutzu S, Castillo PE, Kwon HB. De novo synaptogenesis induced by GABA in the developing mouse cortex. Science. 2016; 353:1037–1040. DOI: 10.1126/science.aaf5206 [PubMed: 27516412]
35. Chen JL, et al. Clustered dynamics of inhibitory synapses and dendritic spines in the adult neocortex. Neuron. 2012; 74:361–373. DOI: 10.1016/j.neuron.2012.02.030 [PubMed: 22542188]
36. Villa KL, et al. Inhibitory Synapses Are Repeatedly Assembled and Removed at Persistent Sites In Vivo. Neuron. 2016; 90:662–664. DOI: 10.1016/j.neuron.2016.03.035
37. Li Y, et al. Orexins in the paraventricular nucleus of the thalamus mediate anxiety-like responses in rats. Psychopharmacology (Berl). 2010; 212:251–265. DOI: 10.1007/s00213-010-1948-y [PubMed: 20645079]
38. Takada M, Campbell KJ, Moriizumi T, Hattori T. On the origin of the dopaminergic innervation of the paraventricular thalamic nucleus. Neurosci Lett. 1990; 115:33–36. [PubMed: 1699175]
39. Uematsu A, et al. Modular organization of the brainstem noradrenaline system coordinates opposing learning states. Nat Neurosci. 2017; 20:1602–1611. DOI: 10.1038/nn.4642 [PubMed: 28920933]
40. Berridge CW, Waterhouse BD. The locus coeruleus-noradrenergic system: modulation of behavioral state and state-dependent cognitive processes. Brain Res Brain Res Rev. 2003; 42:33–84. [PubMed: 12668290]

41. Martins AR, Froemke RC. Coordinated forms of noradrenergic plasticity in the locus coeruleus and primary auditory cortex. Nat Neurosci. 2015; 18:1483–1492. DOI: 10.1038/nn.4090 [PubMed: 26301326]

42. Schmitt LI, et al. Thalamic amplification of cortical connectivity sustains attentional control. Nature. 2017; 545:219–223. DOI: 10.1038/nature22073 [PubMed: 28467827]

43. Sherman SM. Thalamus plays a central role in ongoing cortical functioning. Nat Neurosci. 2016; 19:533–541. DOI: 10.1038/nn.4269 [PubMed: 27021938]

44. Sherman, SM., Guillery, RW. Exploring the thalamus. Academic Press; 2001.

45. McCall JG, et al. CRH Engagement of the Locus Coeruleus Noradrenergic System Mediates Stress-Induced Anxiety. Neuron. 2015; 87:605–620. DOI: 10.1016/j.neuron.2015.07.002 [PubMed: 26212712]

46. Bingham B, et al. Early adolescence as a critical window during which social stress distinctly alters behavior and brain norepinephrine activity. Neuropsychopharmacology. 2011; 36:896–909. DOI: 10.1038/npp.2010.229 [PubMed: 21178981]

47. Curtis AL, Lechner SM, Pavcovich LA, Valentino RJ. Activation of the locus coeruleus noradrenergic system by intracoerulear microinfusion of corticotropin-releasing factor: effects on discharge rate, cortical norepinephrine levels and cortical electroencephalographic activity. J Pharmacol Exp Ther. 1997; 281:163–172. [PubMed: 9103494]

48. Skirzewski M, et al. ErbB4 signaling in dopaminergic axonal projections increases extracellular dopamine levels and regulates spatial/working memory behaviors. Mol Psychiatry. 2017

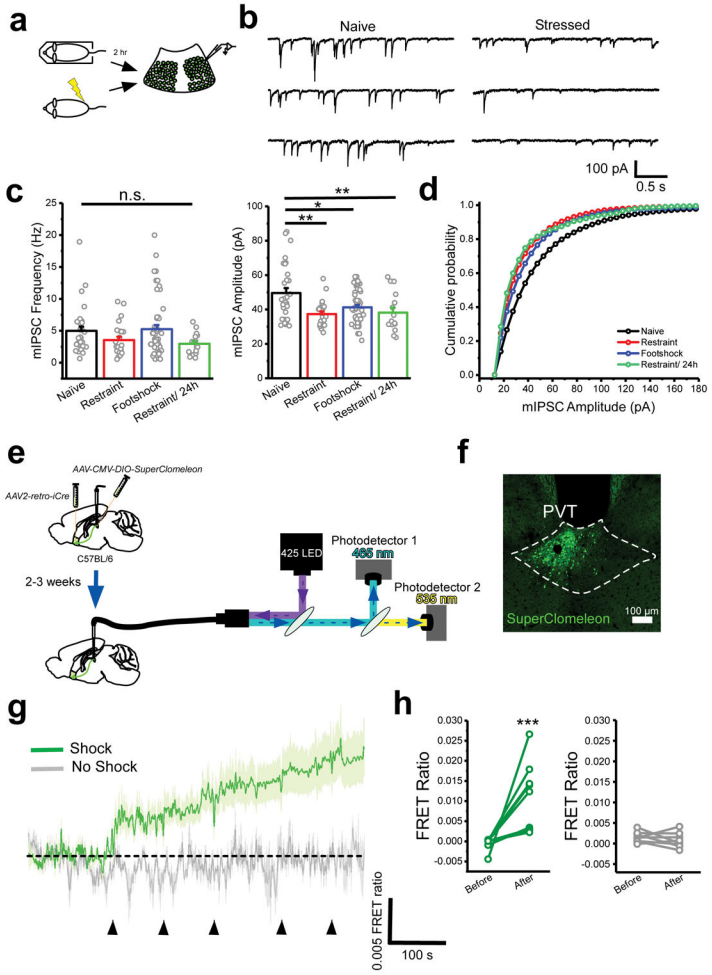

Figure 1. Synaptic inhibition in the pPVT rapidly decreases following stress

a. Schematic of the approach for individually assessing the effect of footshock and restraint stress on synaptic inhibition in $D2^+$ neurons of the pPVT. **b.** Sample mIPSC traces obtained from $D2^+$ neurons of naïve (left panels) and stressed (right panels) mice. **c.** Quantification of mIPSC amplitude (right) and frequency (left). Amplitude in pA, *naïve*, 49.55 ± 2.90, n = 31 neurons, 4 mice; *restraint*, 37.35 ± 1.50, n = 24 neurons, 4 mice; *footshock*, 41.30 ± 1.85, n = 51 neurons, 4 mice; *restraint/24h*, 38.15 ± 2.88, n = 16 neurons, 2 mice; $F_{(3,97)} = 5.80$, one-way analysis of variance (ANOVA) followed by Tukey's test. Group comparisons: *naïve* vs *restraint*, $^{**}P=0.0011$; *naïve* vs *footshock*, $^{*}P=0.012$; *naïve* vs *restraint/24h* $^{**}P=0.01$. Frequency in Hz, *naïve*, 4.99 ± 0.67, n = 31 neurons; *restraint*, 3.54 ± 0.52, n = 24 neurons; *footshock*, 5.25 ± 0.65, n = 30 neurons; *restraint/24h*, 2.97 ± 0.42, n = 16 neurons; $F_{(3,97)} = 2.08$, one-way ANOVA followed by Tukey's test. Group comparisons: *naïve* vs *restraint*, non-significant $P=0.50$; *naïve* vs *footshock*, non-significant $P=0.99$; *naïve* vs *restraint/24h* non-significant $P=0.31$. **d.** Cumulative probability distribution of mIPSC amplitude. **e.** Schematic of the experimental design used for fiber photometry chloride imaging of NAc-projecting pPVT neurons. **f.** Representative image of SuperClomeleon expression in NAc-projecting neurons of the pPVT. **g.** Average SuperClomeleon response from NAc-projecting pPVT neurons in animals subjected to footshocks. Individual footshocks depicted by

arrowheads. **h.** Average change in baseline fluorescence following footshock stress (left) and no shock (right) shown as FRET ratio x 10^{-3} (*footshock: Before*, −0.50 ± 0.51; *After*, 10.73 ± 2.84; ***P*=0.007, two-sided Paired sample t-test; *no shock: Before*, 1.48 ± 1.35; *After*, 1.52 ± 4.11; n = 9 mice; *P*=0.35, two-sided Paired sample t-test). Data shown as mean ± s.e.m.

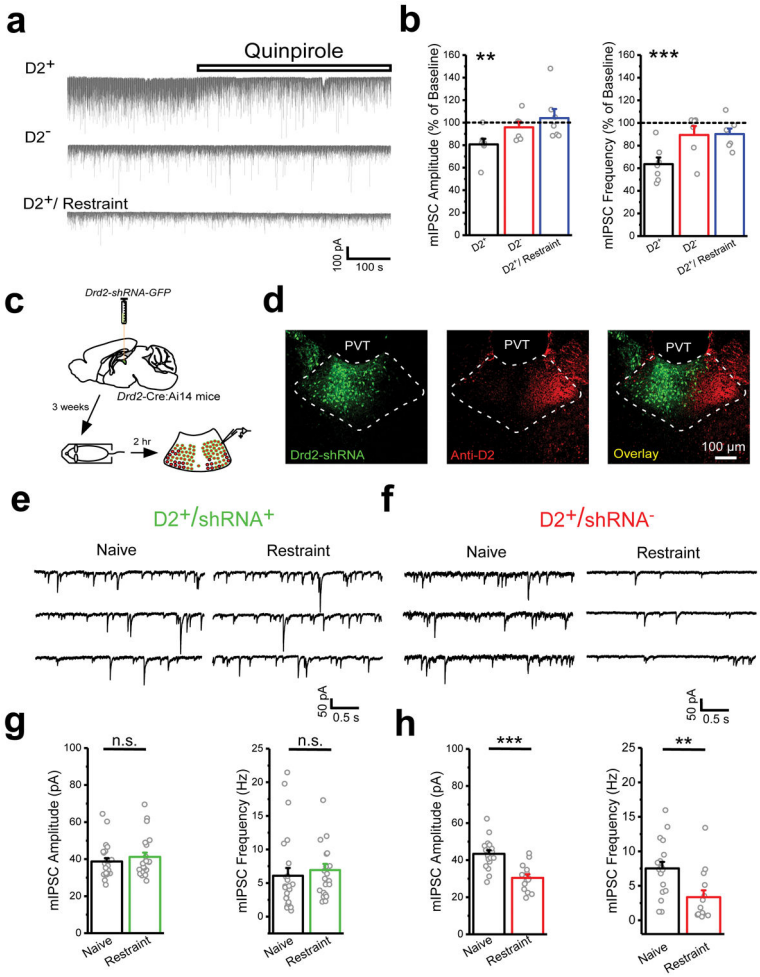

Figure 2. Activation of D2-like dopamine receptors both mimics and is required for stress-induced downregulation of inhibitory transmission

a. Representative traces showing the effect of the D2-like agonist quinpirole (10 μM) on the amplitude and frequency of mIPSC recorded from $D2^+$ (top) and $D2^-$ (middle) neurons of the pPVT of naïve mice, and $D2^+$ neurons of the pPVT of restraint (bottom) mice. **b.** Percent of baseline of mIPSC amplitude (left) and frequency (right) following bath application of quinpirole in $D2^+$ (black) and $D2^-$ (red) neurons of the pPVT of naïve mice, and $D2^+$ neurons of the pPVT of restraint mice (blue). Amplitude percent of baseline, $D2^+$, 80.71 ± 4.94, n = 7 neurons, 4 mice, $^{**}P$=0.008, two-sided Paired sample t-test; $D2^-$, 95.77 ± 4.90, n = 6 neurons, 2 mice, P=0.43, two-sided Paired sample t-test; $D2^+$/*restraint*, 104.01 ± 8.07, n = 7 neurons, 4 mice, P=0.64, two-sided Paired sample t-test. Frequency percent of baseline, $D2^+$, 63.53 ± 5.87, n = 7 neurons, 4 animals, $^{***}P$=0.0008, two-sided Paired sample t-test; $D2^-$, 89.37 ± 7.87, n = 6 neurons, 6 animals, P=0.24, two-sided Paired sample t-test; $D2^+$/*restraint*, 90.17 ± 4.78, n = 7 neurons, 4 animals, P=0.10, two-sided Paired sample t-test. **c.** Schematic of the experimental design used to determine the contribution of $D2^+$ receptors of the pPVT to stress-induced reduction in GABAergic transmission. **d.** Representative images of Drd2-shRNA-GFP expression in the pPVT and immunohistochemical assessment of D2 protein via antibody staining (knockdown

efficiency = 60% [See Methods]; n = 4 mice). **e.** Sample mIPSC traces obtained from shRNA-expressing $D2^+$ neurons ($D2^+$/$shRNA^+$) of naïve (left panels) and stressed (right panels) knockdown mice. **f.** Sample mIPSC traces obtained from shRNA-negative $D2^+$ neurons ($D2^+$/$shRNA^-$) of naïve (left panels) and stressed (right panels) knockdown mice. **g.** Quantification of mIPSC amplitude (left) and frequency (right) from $D2^+$/$shRNA^+$ neurons. Amplitude in pA, *naïve*, 38.73 ± 1.79, n = 23 neurons, 4 mice; *restraint*, 42.27 ± 2.48, n = 25 neurons, 3 mice; non-significant, P=0.40; two-sided t-test. Frequency in Hz, *naïve*, 6.10 ± 1.15, n = 23 neurons, 4 mice; *restraint*, 7.54 ± 0.52, n = 25 neurons, 3 mice; non-significant, P=0.58; two-sided t-test. **h.** Quantification of mIPSC amplitude (left) and frequency (right) from $D2^+$/$shRNA^-$ neurons. Amplitude in pA, *naïve*, 43.41 ± 1.91, n = 18 neurons, 3 mice; *restraint*, 30.43 ± 1.94, n = 14 neurons, 3 mice; ***P=0.00005; two-sided t-test. Frequency in Hz, *naïve*, 7.52 ± 0.96, n = 18 neurons, 3 mice; *restraint*, 3.73 ± 0.99, n = 14 neurons, 3 mice; **P=0.006; two-sided t-test. Data shown as mean ± s.e.m.

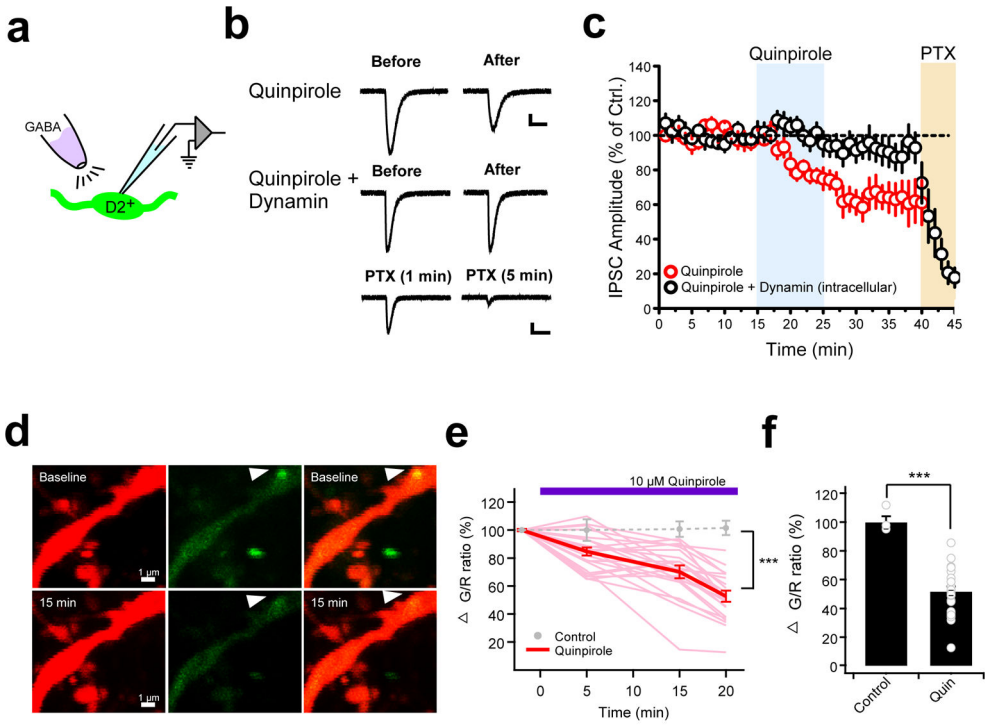

Figure 3. Postsynaptic mechanisms contribute to stress-induced inhibitory plasticity in the pPVT

a. Schematic showing GABA puff experiment assessing postsynaptic involvement in quinpirole-induced GABAergic plasticity in $D2^+$ neurons of the pPVT. **b.** Representative GABA-evoked responses from before and after bath application of quinpirole in the absence (top) and presence (middle) of intracellular dynamin. **c.** Average plot depicting the effect of quinpirole on GABA-evoked responses (n = 9, 6 mice). Note that the effect of quinpirole is prevented in neurons in which the dynamin inhibitory peptide (1 μM) was dialyzed through the patch pipette (n = 9, 4 mice). Bath application of picrotoxin (PTX) confirmed that postsynaptic responses were mediated by $GABA_A$ receptors. **d.** Representative two-photon images of a pPVT neuron dendrite expressing tdTomato (red, left) and Teal-gephyrin (green, middle) in both the absence (baseline, upper) and the presence (15 min, bottom) of 10 μM quinpirole. Arrowhead indicates a gephyrin-positive punctum whose fluorescence decreases following bath application of quinpirole. **e.** Changes in green/red (G/R) ratio at gephyrin puncta over time (light red, individual traces with quin; red, averaged trace with quin; gray circles, average without quinpirole). Difference between control and quinpirole: at 5 min P=0.051, at 15 min P=0.0046, and at 20 min P=0.000012; two-sided t-test. **f.** Summary bar graph of the change of G/R ratio before and 20 min after 10 μM quinpirole (Control: 100 ± 0.8%, n = 4 cells, 4 mice; Quinpirole: 52.8 ± 4.1%, n = 23 cells, 10 mice; *** P= 0.000012; two-sided t-test). Data shown as mean ± s.e.m.

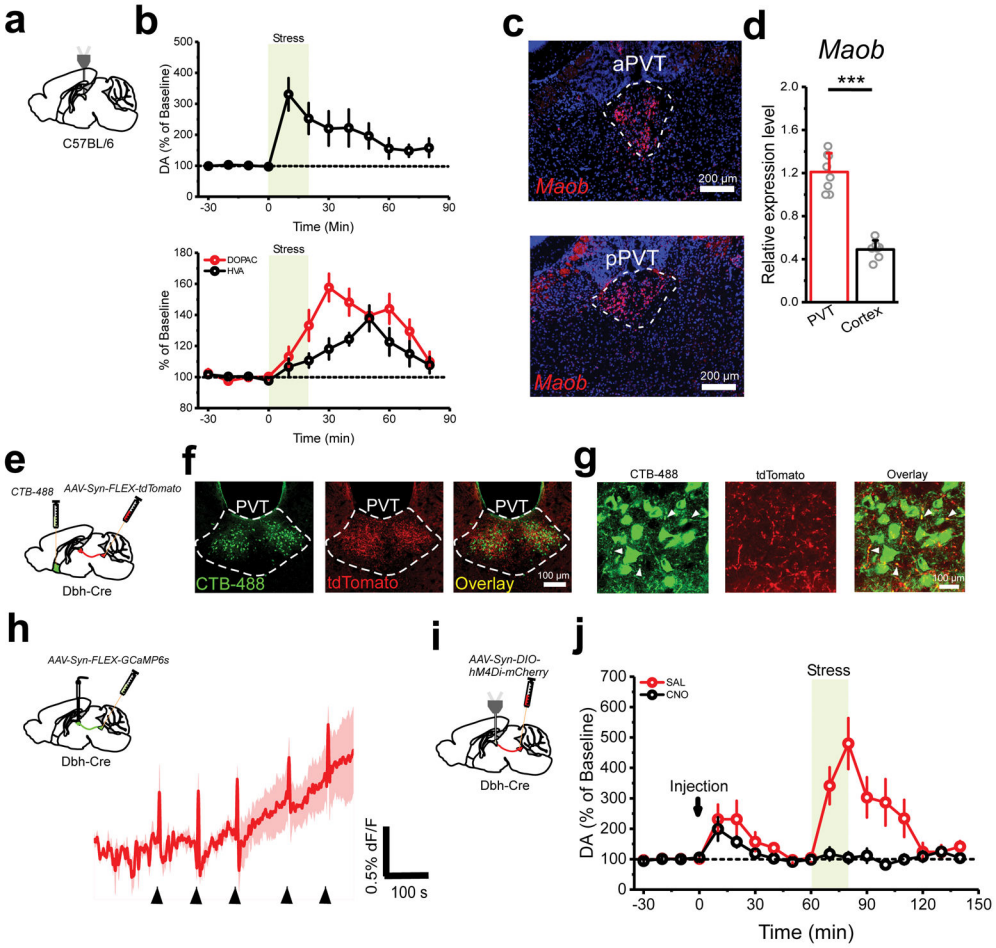

Figure 4. The LC drives stress-evoked dopamine release in the pPVT

a. Schematic microdialysis of the pPVT following stress. Importantly, tail suspension stress was used instead of footshock or restraint due to technical limitations. **b.** Summary plot depicting stress-induced increases in the extracellular concentration of dopamine (DA) (top), as well as the dopamine metabolites 3,4-dihydrixyphenylatic acid (DOPAC) and homovanillic acid (HVA) in the pPVT (bottom) (n = 7 mice). **c.** Fluorescent in situ hybridization experiment showing the expression of monoamine oxidase B (*Maob*) mRNA in both the anterior PVT (aPVT) and the pPVT. **d.** Quantification of the relative expression levels of *Maob* mRNA in the PVT and in cortex (*PVT*, 1.21 ± 0.06; n = 8 mice; *Cortex*, 0.49 ± 0.03; n = 7 mice; *P*=0.0000002; two-sided t-test). **e.** Schematic of the experimental approach used to simultaneously label NAc-projecting neurons and LC neurons terminals in the pPVT. **f.** Representative images showing retrogradely labelled (CTB) NAc-projecting pPVT neurons in the same vicinity as anterogradely labeled (tdTomato) fibers from the LC. This experiment was independently repeated three times and similar results were obtained. **g.** High magnification of the pPVT showing putative synaptic contacts between CTB-labeled neurons and tdTomato-labelled LC afferents. This experiment was independently repeated three times and similar results were obtained. **h.** Average GCaMP6s response from the terminals of LC neurons in the pPVT of animals subjected to footshocks (n = 4 mice). **i.** Schematic of the approach utilized for combined chemogenetic silencing of the LC and

microdialysis of the pPVT. **j.** Summary plot depicting stress-induced increases in the extracellular concentration of dopamine (DA) following CNO (black) and saline vehicle (red) I.P. injection in mice expressing hM4Di in LC (n = 7 mice, per group). Data shown as mean ± s.e.m.

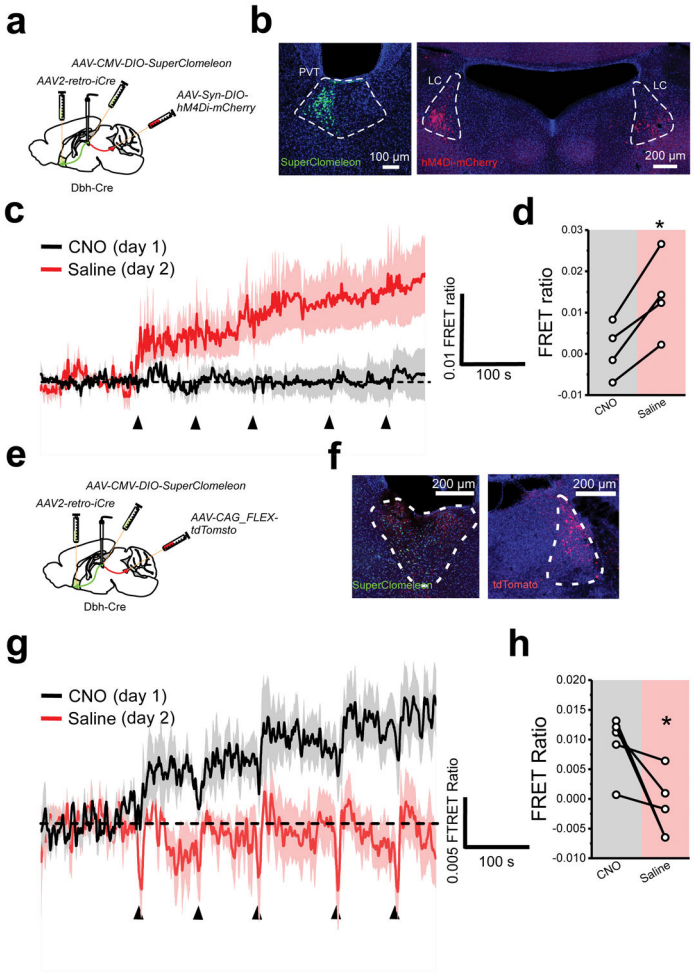

Figure 5. The LC controls stress-induced inhibitory plasticity in the pPVT

a. Schematic of the stereotaxic injections for selectively expressing SuperClomeleon in NAc-projecting neurons of the pPVT and inhibitory DREADD (hM4Di) in catecholaminergic neurons of the LC using *Dbh*-Cre mice. **b.** Representative images showing successful expression of SuperClomeleon and hM4Di-mCherry in the desired targets. Assessment of viral expression was independently repeated four times for this experiment and similar results were obtained. **c.** Average SuperClomeleon response from NAc-projecting pPVT neurons in animals subjected to footshocks in the presence of CNO (day 1; black) or saline (day 2; red). Individual footshocks depicted by arrowheads. **d.** Average change in baseline fluorescence following footshock stress shown as FRET ratio x 10^{-3} (*CNO*, 0.90 ± 3.29; *Saline*, 13.90 ± 5.00; n = 4 mice; *P*=0.013; two-sided t-test). **e.** Schematic of the stereotaxic injections for selectively expressing SuperClomeleon in NAc-projecting neurons of the pPVT and tdTomato in catecholaminergic neurons of the LC using *Dbh*-Cre mice. **f.** Representative images showing successful expression of SuperClomeleon and tdTomato in the desired targets. Assessment of viral expression was independently repeated five times for this experiment and similar results were obtained. **g.** Average SuperClomeleon response from NAc-projecting pPVT neurons in animals subjected to footshocks in the presence of CNO (day 1; black) or Saline (day 2; red). Individual

footshocks depicted by arrowheads. **h.** Average change in baseline fluorescence following footshock stress shown as FRET ratio x 10^{-3} (*CNO*, 9.27 ± 2.24; *Saline*, −1.47 ± 5.44; n = 5 mice; P=0.044; two-sided t-test). Data shown as mean ± s.e.m.

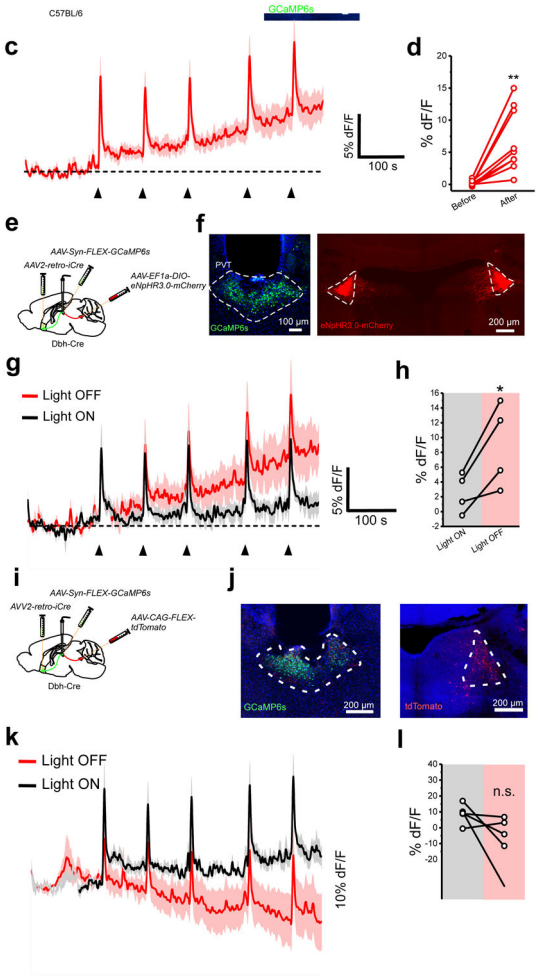

Figure 6. LC input to the pPVT amplify neural responses to stress

a. Schematic of viral vector injections and optical fiber implantation for GCaMP6 fiber photometry experiments. **b.** Representative image of GCaMP6s expression in NAc-projecting neurons of the pPVT and optical fiber placement. **c.** Average GCaMP6s response from NAc-projecting pPVT neurons in animals subjected to footshock stress. Individual footshocks depicted by arrowheads. **d.** Average change in baseline fluorescence following footshock stress in %dF/F (*Before*, 0.15 ± 0.13; *After*, 6.76 ± 1.57; n = 9 mice; *P*=0.003; two-sided Paired sample t-test). **e.** Schematic of the stereotaxic injections for selectively expressing GCaMP6s in NAc-projecting neurons of the pPVT and halorhodopsin in catecholaminergic neurons of the LC using *Dbh*-Cre mice. **f.** Representative images showing successful expression of GCaMP6s and halorhodopsin in the desired targets. Assessment of viral expression was independently repeated four times for this experiment and similar results were obtained. **g.** Average GCaMP6s response from NAc-projecting pPVT neurons in animals subjected to footshocks in the presence (black) and absence (red) of light stimulation. Individual footshocks depicted by arrowheads. **h.** Average change in baseline fluorescence following footshock stress in %dF/F (*Light ON*, 2.57 ± 1.32; *Light OFF*, 8.93 ± 2.84; n = 4 mice; *P*=0.038; two-sided t-test). **i.** Schematic of the stereotaxic injections for selectively expressing GCaMP6s in NAc-projecting neurons of the pPVT and tdTomato in

catecholaminergic neurons of the LC using *Dbh*-Cre mice. **j.** Representative images showing successful expression of GCaMP6s and tdTomato in the desired targets. Assessment of viral expression was independently repeated four times for this experiment and similar results were obtained. **k.** Average GCaMP6s response from NAc-projecting pPVT neurons in animals subjected to footshocks in the presence (black) and absence (red) of light stimulation. Individual footshocks depicted by arrowheads. **l.** Average change in baseline fluorescence following footshock stress in %dF/F (*Light ON*, 8.85 ± 2.77; *Light OFF*, −8.48 ± 7.74; n = 5 mice; non-significant, P=0.10; two-sided t-test). Data shown as mean ± s.e.m.

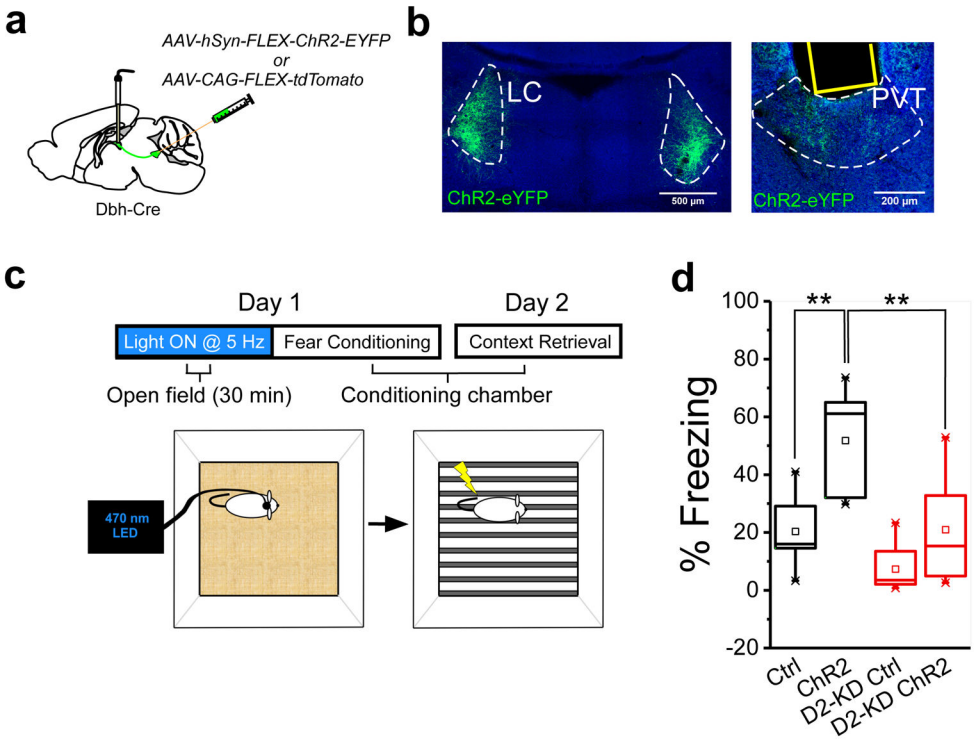

Figure 7. Optogenetic stimulation of LC terminals in the pPVT prior to stress, enhances aversive memory formation

a. Schematic of ChR2-expressing viral vector injections and optical fiber implantation for optogenetic activation of ChR2$^+$ LC fibers in the pPVT. **b.** Representative image of ChR2 expression in the LC of *Dbh*-Cre mice and ChR2$^+$ terminals in the pPVT. Assessment of viral expression was independently repeated fourteen times for this experiment (7 mice with ChR2 and 7 mice with ChR2 + Drd2-shRNA) and similar results were obtained. **c.** Schematic of the experimental setup for optogenetic stimulation of LC terminals in the pPVT (5Hz for 30) prior to fear conditioning (5 shocks, 0.4 mA). Fear memory to the conditioning context was tested the following day for both ChR2$^+$ and control mice. **d.** Summary plot of freezing behavior during the fear memory retrieval for both ChR2$^+$ and control mice. Quantification of freezing behavior during the fear memory retrieval for both D2 receptor intact (black boxes) and D2 receptor knockdown (D2 KD; red boxes) mice subjected to optogenetic stimulation of LC terminals in the pPVT. Percent of freezing, *Ctrl*, 20.34 ± 4.57, n = 7 mice; *ChR2*, 51.77 ± 6.77, n = 7 mice; *D2 KD-Ctrl*, 17.24 ± 10.31, n = 7 mice; *D2 KD-ChR2*, 20.94 ± 7.01, n = 7 mice; $F_{(3,24)} = 11.36$, two-way ANOVA followed by Tukey's test. Group comparisons: *Ctrl* vs *ChR2*, $^{**}P=0.003$; *D2-KD Ctrl* vs *D2-KD ChR2*, $P=0.33$; ChR2 vs D2-KD ChR2, **P=0.004. Box chart legend: box is defined by 25th, 75th percentiles, whiskers are determined by 5th and 95th percentiles, and mean is depicted by the square symbol. Data shown as mean ± s.e.m.